Feng et al. *NPG Asia Materials* (2018) 10: 800–809
DOI 10.1038/s41427-018-0072-z

NPG Asia Materials

ARTICLE Open Access

A general ligand-assisted self-assembly approach to crystalline mesoporous metal oxides

Danyang Feng[1], Tu-Nan Gao[1], Meihong Fan[1], Ang Li[1], Kaiqian Li[1], Tao Wang[1], Qisheng Huo[1] and Zhen-An Qiao[1]

Abstract

Mesoporous transition metal oxides with high crystallinity and large pore volumes were successfully synthesized by a widely applicable ligand-assisted self-assembly approach. In this approach, a carboxyl-containing ligand is employed as a coordination agent to retard the hydrolysis and condensation rates of the precursors. The ligands interact with the PEO chains of P123 via hydrogen bonds, which cooperatively ensures the controllable co-assembly of template micelles and the metal source during solvent evaporation. The X-ray diffraction, transmission electron microscopy, and nitrogen sorption results show that the obtained mesoporous metal oxides are constructed from numerous highly crystalline nanoparticles and possess close-packed mesostructures with uniform pore size distributions. A series of mesoporous transition metal oxides (Co_3O_4, Mn_2O_3, Fe_3O_4, NiO, CuO, ZnO, and Cr_2O_3) and multi-metal oxide composite materials (Co_3O_4/Fe_3O_4, Co_3O_4/NiO, and Fe_3O_4/NiO) were successfully synthesized. By employing the crystalline Co_3O_4/Fe_3O_4 composites as electrocatalysts, high catalytic activity can be achieved during the oxygen evolution reaction. A low overpotential of 322 mV at a current density of 10 mA cm^{-2} is exhibited, which shows that this approach has great significance not only in synthesis but also in electrocatalysis.

Introduction

Mesoporous transition metal oxides possessing a large surface area and high degree of crystallization have attracted extensive attention because of their remarkable properties and promising applications in gas sensing, energy storage, catalysis, and photodetection[1–8]. Various strategies have been used to synthesize mesoporous transition metal oxides. One promising route is the hard template approach, which employs mesoporous silica or carbon as a rigid template to introduce the desired mesoporous structure and removes the template by etching or calcination to finally obtain mesoporous transition metal oxides[9–12]. This approach can synthesize unique crystalline and ordered mesoporous metal oxides but still has some deficiencies. For example, the mesoporous structures of the metal oxides depend on the frameworks of the hard templates, and only a few hard templates are available for use. Moreover, the procedure is costly, laborious, and low yielding. To overcome these limitations, a soft-templating approach was proposed, i.e., the evaporation-induced self-assembly (EISA) route. For instance, Fan et al. prepared multicomponent mesoporous metal oxides in a versatile sol–gel solution consisting of acetic acid[13]. Suib et al. reported an inverse micelle synthesis system to prepare mesoporous metal oxides[14]. Mesoporous materials with diverse morphologies and tunable pore sizes have been prepared by controlling the synthesis conditions and the properties of the template molecules based on soft templating[15,16]. This approach is flexible and effective for large-scale synthesis. However, the mesostructures are apt to shrink and even collapse during formation of the mesostructure by calcination and removal of the organic templates. The pore walls of mesoporous transition metal oxides formed by the soft-templating approach are almost amorphous or semi-crystalline, which may impede their

Correspondence: Zhen-An Qiao (qiaozhenan@jlu.edu.cn)
[1]State Key Laboratory of Inorganic Synthesis and Preparative Chemistry, College of Chemistry, Jilin University, Changchun, Jilin 130012, China

further applications. Moreover, uncontrolled hydrolysis and condensation of transition metal sources, such as alkoxides, can result in poorly structured materials due to the rapid formation of dense, cross-linked inorganic networks. Carboxylic acid-containing ligands can be used as structure-directing agents in soft-templating approaches[17,18], and the ligand-assisted EISA method developed by Deng and coauthors provides a new idea for the synthesis of stable and crystalline mesoporous oxides[19]. Although great advances have been made in the synthesis of several mesoporous transition metal oxides, the development of a universal method to synthesize thermally stable and highly crystalline mesoporous metal oxides is still a great challenge.

Herein, we demonstrate a general effective ligand-assisted self-assembly synthesis strategy to prepare mesoporous transition metal oxides composed of highly crystalline nanocrystals with high surface area and unique stability by using the triblock copolymer P123 as a template, metal nitrate as a precursor, and acidic n-butanol as the reaction medium. Remarkably, mesoporous transition metal oxides were prepared by coordinating the metal precursors with carboxyl-containing ligands to control the hydrolysis and condensation rates and decrease the degree of cross-linking of the metal gel networks. Meanwhile, the ligand molecules attached to the PEO chains through H-bonds hinder the local motion of the PEO chains. The slow assembly between template micelles and the inorganic metal source allows the formation of well-defined mesostructures. This general method was successfully used to synthesize a series of mesoporous transition metal oxides, including mesoporous Cr_2O_3, Mn_2O_3, Fe_3O_4, Co_3O_4, NiO, CuO, and ZnO. It is worth mentioning that mesoporous CuO and Cr_2O_3 are both obtained for the first time without using a hard template. Additionally, mesoporous multi-metal oxide composites (e.g., Co_3O_4/Fe_3O_4, Co_3O_4/NiO, and Fe_3O_4/NiO) can also be acquired by this versatile strategy. Excellent electrochemical performance was observed due to the existence of mesoporous structures in these materials. The as-synthesized Co_3O_4 and Co_3O_4/Fe_3O_4 composites are highly active materials for the electrocatalytic oxygen evolution reaction (OER).

Materials and methods

Synthesis of mesoporous metal oxides

All the mesoporous metal oxides were synthesized by the ligand-assisted self-assembly process using citric acid/ascorbic acid as a chelating agent, concentrated HNO_3 to adjust the pH, and n-butanol as a solvent. Metal nitrate and the triblock copolymer Pluronic P123 were employed as the precursor and the template, respectively. In a typical synthesis of mesoporous Co_3O_4, 1.36×10^{-4} mol of P123, 5 mmol of citric acid, and 16 mmol of concentrated HNO_3 were dissolved in 70 mmol of 1-butanol solution under magnetic stirring followed by the addition of 2.5 mmol of the inorganic source $Co(NO_3)_2{\cdot}6H_2O$. The mixture was stirred vigorously for several hours at room temperature until a transparent sol formed. The sol was transferred into a Petri dish (diameter 90 mm), and the solvent was evaporated in a 120 °C oven over 4 h. Then, the as-synthesized pink powder product was removed and calcined in air by a stepwise pyrolysis approach at 150 °C for 4 h (ramp rate 2 °C/min), 250 °C for 2 h (ramp rate 2 °C/min), and 350 °C for 2 h (ramp rate 2 °C/min), resulting in the highly crystalline mesoporous Co_3O_4 product.

Fabrication of the oxygen evolution reaction working electrode

Ten milligrams of catalyst powder was dispersed in 300 μL of isopropyl alcohol and ultrasonically mixed for ~30 min. One microliter of the obtained catalyst slurry was dropped on a polished GC electrode, and then, 2 μL of Nafion (5 wt% in ethanol, Alfa Aesar) was cast onto the above coating and dried in air at room temperature (this yielded an approximate metal loading of 0.5 mg cm^{-2}).

Characterization

Field-emission transmission electron microscopy (TEM), high-resolution TEM (HRTEM), and selected-area electron diffraction (SAED) images were obtained using a FEI Tecnai G2 F20 s-twin D573 field-emission TEM operated at 200 kV. EDX spectra were acquired using a Phillips CM200 TEM instrument (200 kV). Powder X-ray diffraction (XRD) patterns were collected on a Rigaku 2550 diffractometer with Cu Kα radiation at 40 kV and 100 mA ($\lambda = 1.5418$ Å). N_2 adsorption–desorption isotherms were measured at −196 °C on a NOVA 4200e. Samples were degassed at 120 °C for a minimum of 4 h prior to analysis. The specific surface area and pore size distributions were calculated using the Brunauer–Emmett–Teller (BET) equation and the Barrett–Joyner–Halenda (BJH) model from the adsorption branches. Thermogravimetric analysis (TGA) was performed on a TGA Q500 thermogravimetric analyzer in air over the temperature range of 30–800 °C at a heating rate of 10 °C min^{-1}. Inductively coupled plasma emission spectroscopy was carried out using an ICP-OES, PerkinElmer OPTIMA 3300DV. Infrared (IR) spectra were recorded using a Nicolet Impact 410 FTIR spectrometer over the wavelength range of 400–4000 cm^{-1} using KBr pellets.

Electrochemical measurements were performed on a corrected electrochemical workstation (CHI660E) in a conventional three-electrode system containing a 1 M KOH electrolyte. The coated glassy carbon disk electrode (3-mm diameter, disk: 0.071 cm^2) served as the working electrode. A Hg/HgO electrode and high-surface-area Pt mesh were used as the reference and counter electrodes,

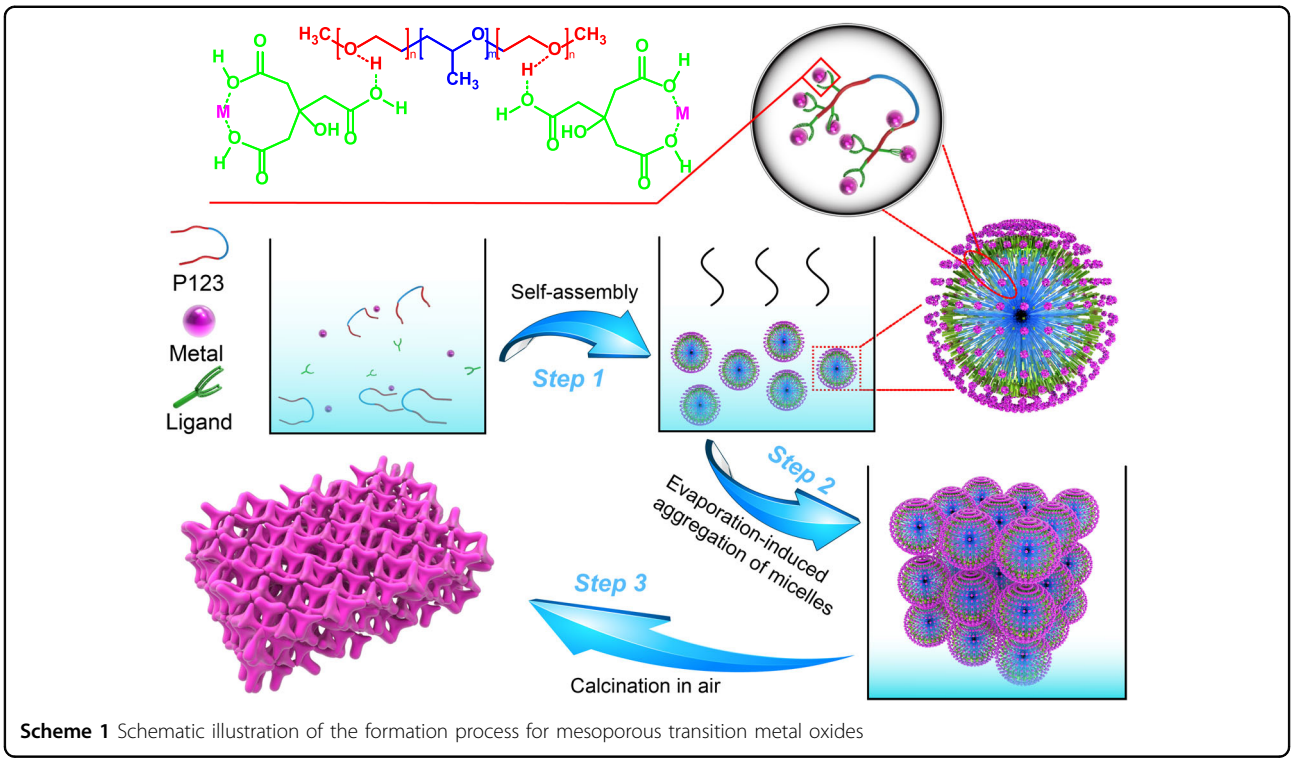

Scheme 1 Schematic illustration of the formation process for mesoporous transition metal oxides

respectively. Linear sweep voltammetry (LSV) curves of different catalysts at scan rates of 5 mV s^{-1} were obtained in 1 M KOH electrolyte over a potential window of 0.296–0.800 V, and the voltage was corrected according to the iR loss from the solution resistance.

Results and discussion

Scheme 1 shows a schematic illustration of the fabrication process of the crystalline mesoporous transition metal oxides. The homogeneous mesostructure was prepared by assembling the carboxyl-coordinated inorganic precursors with an amphiphilic surfactant via a ligand-assisted self-assembly route. In the first stage, inorganic species were dissolved in an acidic n-butanol/P123/carboxylic ligand mixture solution, and then, the obtained transparent sol was dried in an oven for several hours. In this process, the strong aqueous acid HNO_3 was used as the charge intermediate between the inorganic metal clusters and surfactants to hinder condensation. The carboxyl-coordinated transition metal complex was fabricated as an optimized precursor, which effectively retarded the hydrolysis and condensation rates. Due to the existence of coordination bands, the inorganic metal sources were stabilized over the growth period, which led to controllable co-assembly between the precursors and surfactant micelles[20]. In addition, the ligands interacted with the PEO chains of P123 through direct hydrogen bonds between the carboxylic hydroxyl groups and the ether groups of PEO[21]. During the continuous evaporation of n-butanol, mesostructures were gradually formed by both coordination-bonding interactions and hydrogen-bonding interactions. By removing the triblock copolymer templates after a series of calcination processes in air, the crystalline mesoporous transition metal oxides were finally obtained.

The scheme was confirmed by the Fourier transform-infrared (FTIR) spectrum. Taking the synthesis of Co_3O_4 as an example, the C=O vibrational peaks for uncoordinated carboxylic acid appear at 1707 cm^{-1} and 1753 cm^{-1} (Fig. 1e black line), while the C=O vibrational peaks for the coordinated sample appear at 1386 cm^{-1}, 1618 cm^{-1}, and 1738 cm^{-1} (Fig. 1e blue line). The bands at 1386 cm^{-1} and 1618 cm^{-1} can be attributed to the asymmetric and symmetric stretching vibrations of the coordinated carboxylate group. The band at 1738 cm^{-1} can be assigned to the C=O stretching mode of the nondissociated carboxylate group. Moreover, for the coordinated sample, the O–H vibrational peaks of –COOH at ~3500 cm^{-1} and 2600 cm^{-1} (Fig. 1e black line) almost disappeared. The above observations suggest that the O–H bands of the carboxyl groups were partly deprotonated and the carboxyl groups coordinated to the Co atoms. After thermal oxidation in air, the strong adsorption bands at 650 cm^{-1} and 569 cm^{-1} (Fig. 1e red line) can be assigned to the vibration of Co–O in cobalt oxide, confirming that the conversion process involves the transition from the intermediate cobalt carbonate to cobalt oxide through decomposition[22].

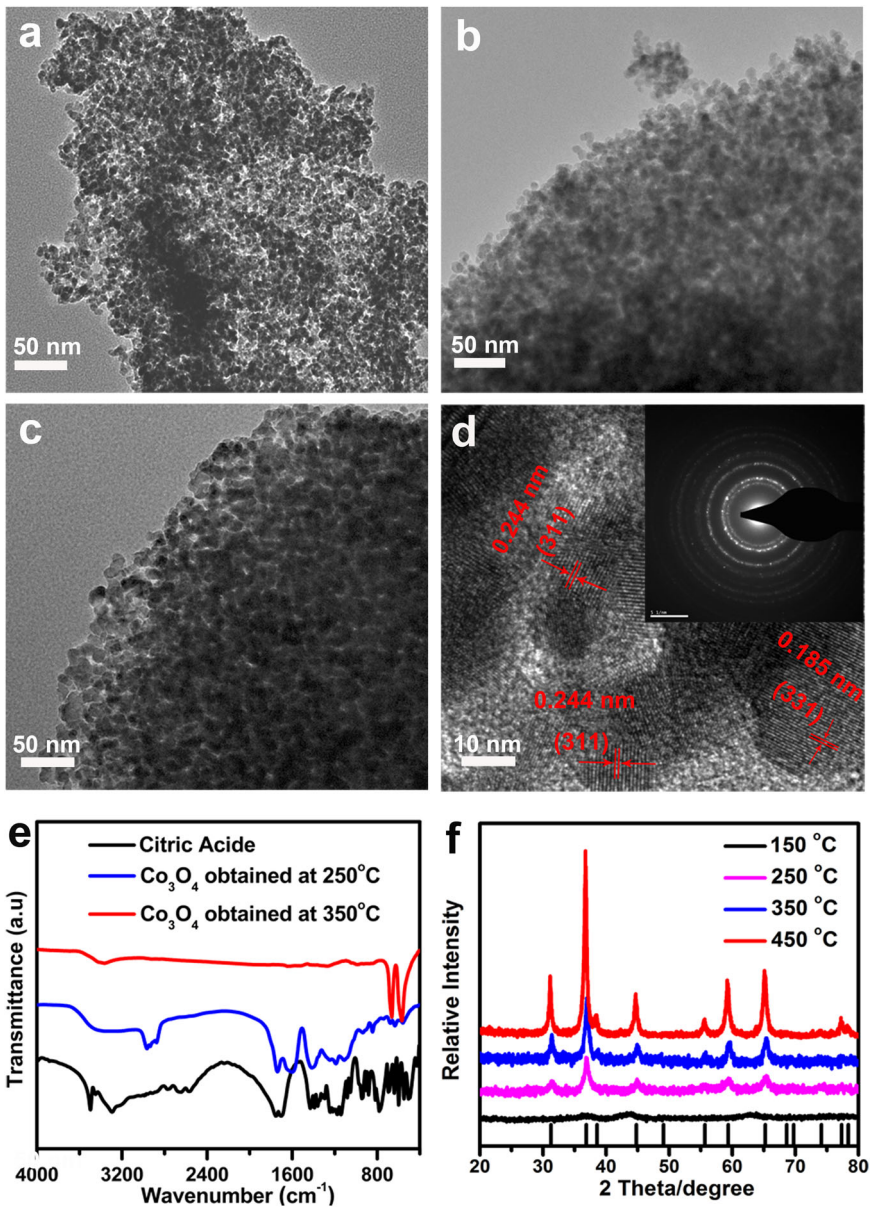

Fig. 1 Characterization of mesoporous Co_3O_4. TEM images of mesoporous Co_3O_4 obtained at (**a**) 250 °C, (**b**) 350 °C, and **c** 450 °C. **d** HRTEM images of mesoporous Co_3O_4 obtained at 350 °C and the corresponding SAED pattern shown in the inset. **e** FTIR spectra of citric acid and mesoporous Co_3O_4. **f** XRD patterns of mesoporous Co_3O_4 at different calcination temperatures

The crystal phase of Co_3O_4 was confirmed by power X-ray diffraction (PXRD). Figure 1f shows the evolution from the amorphous to the crystalline phase with an increase in calcination temperature from 150 °C to 450 °C. The sample calcined at 250 °C shows low crystallinity. After calcination at 350 °C, the XRD pattern displays well-resolved characteristic diffraction peaks, which can be well indexed to cobalt oxide with lattice parameters of $a = 0.8048$ nm, $b = 0.8048$ nm, $c = 0.8048$ nm, and $\beta = 90°$ (JCPDS No. 43-1003), confirming the formation of a highly crystalline phase. Increasing the calcination temperature to 450 °C causes additional crystal growth as well as further improvement in crystallinity. In addition, no characteristic peaks from other crystalline phases were detected, demonstrating the high purity of Co_3O_4. To investigate the morphology and mesostructural information, the as-synthesized samples were characterized by TEM and HRTEM. The walls of the mesopores are composed of ultra-small Co_3O_4 nanocrystals, and the nanocrystals gradually grow as the temperature increases from 250 °C to 450 °C (Fig. 1a–c). As shown in Fig. 1b, Co_3O_4 nanoparticles calcined at 350 °C possess a uniform

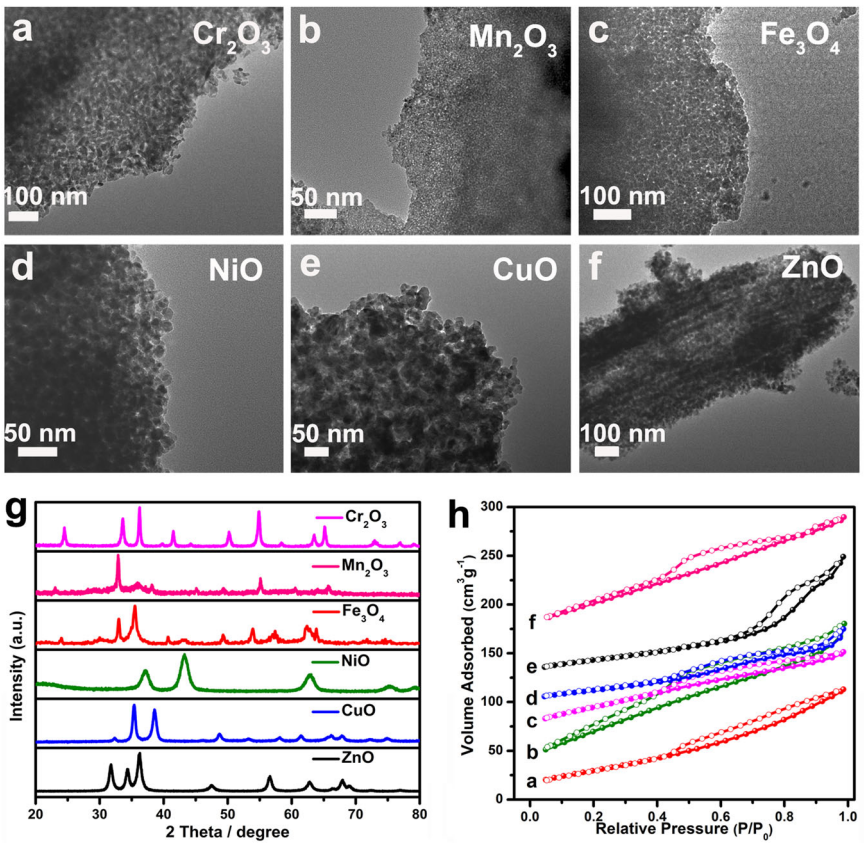

Fig. 2 Characterization of other mesoporous materials. a–f TEM images of different mesoporous transition metal oxides obtained at 350 °C. **g** XRD patterns of different mesoporous transition metal oxides obtained at 350 °C. **h** N_2 adsorption–desorption isotherms of different mesoporous transition metal oxides obtained at 350 °C. **a**–**f** correspond to Fe_3O_4, NiO, Cr_2O_3, CuO, ZnO, and Mn_2O_3. The isotherm curves (**b**, **c**, **d**, **e**,) and **f** in **h** are shifted by 30, 60, 90, 120, and 150 $cm^3 g^{-1}$, STP, respectively, for clarity

size distribution of approximately 6 nm, which is consistent with the result of 6.4 nm calculated by the Scherrer equation (according to Fig. 1f, blue line). The distinct lattice can be clearly observed in the HRTEM image (Fig. 1d), further revealing that the as-synthesized sample is well crystallized. The corresponding SAED, inset in Fig. 1d, shows a set of well-defined concentric rings, which clearly verifies the polycrystalline character of mesoporous Co_3O_4.

The nitrogen sorption–desorption isotherms of mesoporous Co_3O_4 obtained by calcination at different temperatures are shown in Figure S1 and Figure S2. After calcination at 350 °C in air, the isotherms exhibit characteristic type-IV curves with distinct hysteresis loops close to H_2 type, reflecting the existence of mesopores. The BJH adsorption pore diameter (inset in Figure S1) exhibits a narrow peak at 3.4 nm calculated from the adsorption branch, clearly indicating that the mesoporous Co_3O_4 prepared by the ligand-assisted self-assembly method possesses a well-defined and uniform pore size distribution. The corresponding specific surface area and pore volume of this material estimated from the BET method are 106 $m^2 g^{-1}$ and 0.24 $cm^3 g^{-1}$, respectively. As the calcination temperature increased from 350 °C to 450 °C, the specific surface area decreased from 106 $m^2 g^{-1}$ to 32 $m^2 g^{-1}$, while the pore size increased from 3.4 nm to 6.1 nm.

To confirm the versatility of the method, crystalline Cr_2O_3, Mn_2O_3, Fe_3O_4, NiO, CuO, and ZnO with well-defined mesoporous structures were synthesized by this ligand-assisted self-assembly approach. The XRD patterns of the as-prepared samples all match well with their corresponding metal oxide phases (Fig. 2g): eskolaite for Cr_2O_3, hausmannite for Mn_3O_4, bunsenite for NiO, and zinicite for ZnO. The TEM images (Fig. 2a–f) of these samples, obtained at 350 °C, show that all the formed materials maintain their disordered worm-like mesoporous structures, and the walls of mesopores are constructed from small highly crystallized nanocrystals with similar morphological features. A similar two-dimensional pore structure can be observed in the TEM

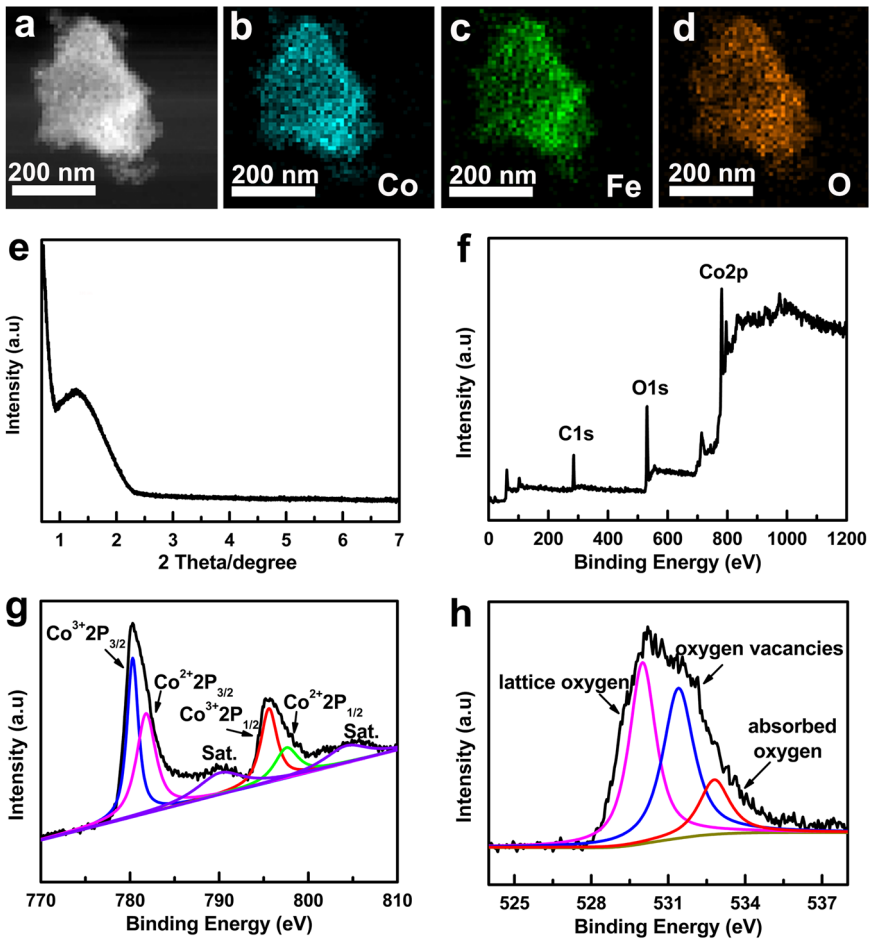

Fig. 3 Component analysis of the mesoporous materials. a Typical STEM image of mesoporous Co_3O_4/Fe_3O_4 (4:1) composites and the corresponding elemental mapping of **b** cobalt, **c** iron, and **d** oxygen elements. **e** Small-angle XRD pattern of ZnO. **f** Survey XPS spectrum of Co_3O_4. **g** High-resolution XPS Co 2p spectrum and **h** high-resolution XPS O 1 s spectrum

image of ZnO, and an individual ZnO channel has a width of 7.8 nm with rough surfaces. In contrast to other metal oxides, ZnO is prepared with ascorbic acid instead of citric acid. Compared with the other mesoporous metal oxides we obtained, the small-angle XRD pattern (Fig. 3e) of ZnO shows a more apparent diffraction between 1° and 2°, indicating a relatively regular mesoporous structure, which is consistent with the TEM results. N_2 adsorption–desorption isotherms and the corresponding pore size distribution curves of the obtained mesoporous transition metal oxides are shown in Fig. 2h and Figure S6. The BET surface areas of the obtained samples are in the range of 68– 205 $m^2 g^{-1}$: 130 $m^2 g^{-1}$ for Cr_2O_3, 205 $m^2 g^{-1}$ for Mn_2O_3, 127 $m^2 g^{-1}$ for Fe_3O_4, 137 $m^2 g^{-1}$ for NiO, 68 $m^2 g^{-1}$ for CuO, and 86 $m^2 g^{-1}$ for ZnO.

This ligand-assisted self-assembly method can also be used for the fabrication of mesoporous materials with multicomponent structures. Mesoporous Co_3O_4/Fe_3O_4, Co_3O_4/NiO, and Fe_3O_4/NiO composites with controlled metal molar ratios were synthesized successfully. The specific surface areas are in a wide range from 87 $m^2 g^{-1}$ to 174 $m^2 g^{-1}$, and the pore volumes ranged from 0.131 $m^3 g^{-1}$ to 0.310 $m^3 g^{-1}$. The small-angle XRD patterns of single- and multi-metal oxides are shown in Figure S4 and Figure S5. Concrete mesostructural data and the corresponding nitrogen sorption–desorption isotherms of these samples are summarized in Table S1 and Figures S7–9. Taking the Co_3O_4/Fe_3O_4 composition as an example, the chemical compositions were verified by XRD (Figure S10). ICP analysis shows that the Co/Fe molar ratio is approximately 4:1, which is in accordance with the initial amount of metal nitrates added during preparation of this composite material. Figure 3a and Figure S11 show the STEM and TEM images of the mesoporous Co_3O_4/Fe_3O_4 (4:1) composites. The corresponding EDX elemental mapping images of Co, Fe, and O (Fig. 3b, c, d) reveal a homogeneous distribution of Co and Fe in the mesoporous framework. We believe that our

ligand-assisted self-assembly approach is a versatile method for the synthesis of both single- and multi-transition metal oxide composites.

The chemical states of Co_3O_4 were examined by X-ray photoelectron spectroscopy (XPS). A survey scan (Fig. 3f) revealed that the surface mainly consists of Co, O, and C. As shown in Fig. 3g, the peaks at ~780.3 and ~795.5 eV can be indexed to Co^{3+} $2p_{1/2}$ and Co^{3+} $2p_{3/2}$, and those located at ~781.8 and ~797.5 eV correspond to Co^{2+} $2p_{1/2}$ and Co^{2+} $2p_{3/2}$, suggesting that two valence states (octahedral Co^{3+} and tetrahedral Co^{2+}) coexist in Co_3O_4. The O 1 s spectrum (Fig. 3h) can be deconvoluted into three distinct peaks: oxygen ions in the crystal lattice (at 530.1 eV), oxygen vacancies (at 532.2 eV), and absorbed oxygen species (at 531.2 eV)[23]. The thermogravimetric analysis trace (Figure S12) obtained after evaporation at 120 °C shows two thermal events: a large weight loss at 180 °C and a smaller weight loss at 350 °C, which correspond to conversion from $CoCO_3$ to Co_3O_4 and the combustion of residual carbon, respectively.

To confirm the positive role of the carboxyl ligand, control experiments without ligands were performed. The surface areas show a dramatic declining trend for some of the transition metal oxides, decreasing from 130 to 26 m^2g^{-1} for Cr_2O_3, from 68 to 16 $m^2 g^{-1}$ for CuO, and from 86 to 31 $m^2 g^{-1}$ for ZnO (Figure S12). In addition, the crystallinity of Mn_2O_3 also decreased. Mn_2O_3 synthesized without the addition of carboxyl ligands is not crystalline until the calcination temperature is increased to 450 °C, while the oxide is already highly crystallized at 350 °C in the presence of carboxyl ligands (Figure S13).

Water electrolysis is considered a promising way to overcome the problem of fossil fuel depletion. Transition metal oxides such as Co_3O_4 and NiO have been regarded as effective catalysts to replace the precious iridium and ruthenium oxides in the OER[24–27]. Here, we assessed the OER properties in a standard three-electrode system. During the electrochemical measurement, oxygen evolved rapidly from the catalyst surface. The overpotential at a current density of 10 mA cm^{-2} is relevant to the water-splitting reaction. Mesoporous Co_3O_4 samples obtained at different temperatures were tested for the OER to confirm the optimal calcination temperature of the electrocatalysts. As shown in Figure S14, the overpotential of mesoporous Co_3O_4 calcined at 350 °C is 353 mV, while Co_3O_4 calcined at 250 °C, possessing lower crystallinity, shows a high overpotential of 466 mV, and Co_3O_4 calcined at 450 °C, possessing higher crystallinity, shows an overpotential of 391 mV. These results demonstrate that the samples calcined at 350 °C show the best performance. To corroborate the existence of mesopores playing an active role in the OER, commercial Co_3O_4 nanoparticles,

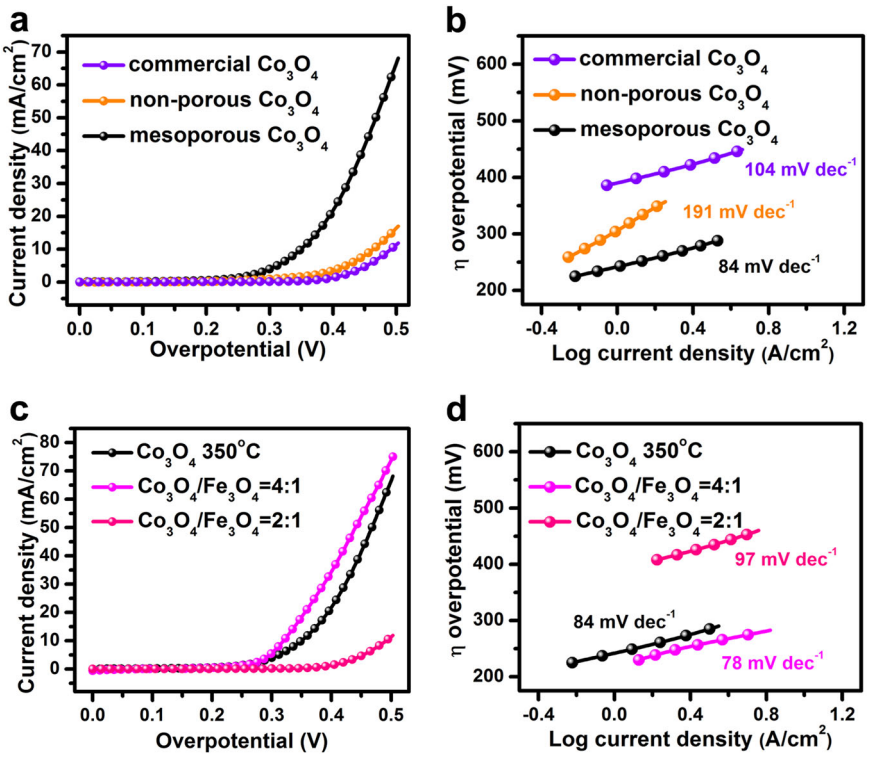

Fig. 4 OER performance of different types of catalysts. a, **b** LSV curves and Tafel plots of different types of Co_3O_4. **c**, **d** LSV curves and Tafel plots of different Co_3O_4/Fe_3O_4 ratios

Table 1 Comparison of catalyst activity in the OER

Catalyst	Mass loading ($\mu g\ cm^{-2}$)	η at J = 10 mA cm^{-2} (mV)	Tafel slope ($mV\ dec^{-1}$)	Mass activity at η = 0.4 V ($A\ g^{-1}$)	TOF at η = 0.4 V (s^{-1})	Ref.
Co_3O_4/Fe_3O_4 (4:1) composites	500	322	78	34.4	0.0215	Our work
Co_3O_4	500	353	84	21.5	0.0314	Our work
Co_3O_4-MNTs	531	353	80	—	—	[28]
Co_3O_4@CoO SC	25	430	89	234.0	0.0487	[29]
$Co_{0.54}Fe_{0.46}OOH$	—	390	47	200 at η = 0.39 V	0.0225	[30]
CoOx-4-h nanoplates	500	306	61	—	0.0030	[31]
Fe_1Co_1-ONS	360	308	36.8	54.9 at η = 0.35 V	0.0214 at η = 0.35 V	[32]

non-porous Co_3O_4 obtained at 650 °C, and mesoporous Co_3O_4 obtained at 350 °C were tested for the OER. As shown in Fig. 4a, the overpotential of commercial Co_3O_4 is 490 mV, and that of non-porous Co_3O_4 is 464 mV, which are both much higher than that of mesoporous Co_3O_4, indicating that mesopores provided the best OER performance. This obvious change can be ascribed to the introduction of porous structures. The mesopores not only contribute more catalytic active sites but also facilitate the detachment of oxygen bubbles from the electrode surface, which cooperatively promote the catalytic activity of Co_3O_4. Figure 4c shows the LSV curves of the pure mesoporous Co_3O_4 and Co_3O_4/Fe_3O_4 composite electrodes calcined at 350 °C. The Co_3O_4/Fe_3O_4 (4:1) composite requires an overpotential of only 322 mV to achieve a current density of 10 mA cm^{-2}, which is superior to most previous reports on non-precious OER electrocatalysts in alkaline aqueous electrolytes (Table 1)[28–32]. For comparison, the Co_3O_4/Fe_3O_4 (2:1) composite demands an overpotential of 494 mV to achieve a current density of 10 mA cm^{-2}, and no obvious current response is observed when the working electrode film is prepared by pure mesoporous Fe_3O_4 (Figure S15). The enhancement of the catalytic performance when going from pure Co_3O_4 to the Co_3O_4/Fe_3O_4 (4:1) composite can be attributed to synergistic effects and interface effects between Co_3O_4 and Fe_3O_4, which promote charge flow in the working electrode and can lead to the efficient transport of electrons and ions in this composite material[33,34]. Furthermore, the difference in the degree of electrolyte infiltration among the different mesoporous materials can also influence the catalytic activity. Under the premise of not changing the predominance of Co_3O_4, the introduction of Fe_3O_4 provides a larger BET (from 106 to 170 m^2/g) and a higher pore volume (from 0.235 to 0.310 cm^3/g), which allows the electrolyte solution to infiltrate into the porous electrode more adequately. However, the catalytic activity of the composite materials decreases with increasing Co/Fe ratio from 4:1 to 2:1, because pure Fe_3O_4 does not show any catalytic activity and excessively increasing the proportion of Fe_3O_4 is not conducive to catalytic activity in the OER. The catalytic activities of other Co/Fe ratios are shown in Figure S16.

To advance our understanding of the enhancement in OER activity, the electrochemically active surface area (ECSA) of the as-prepared catalysts was tested by electrochemical capacitance surface area measurements[35–38]. The ECSA is positively proportional to the double-layer capacitance (C_{dl}) (Fig. 5a, b), which is equivalent to half of the slope. The obtained capacitive currents are plotted as a function of the scan rate in Fig. 5c. The capacitance of Co_3O_4/Fe_3O_4 (4:1) was calculated to be 144.7 mF cm^{-2}, which is higher than that of mesoporous Co_3O_4 (83.7 mF cm^{-2}). The results suggest that more exposed active sites are available for Co_3O_4/Fe_3O_4 (4:1), which contribute to better electrocatalytic performance.

The catalytic OER kinetics of the catalysts were investigated using Tafel plots (log j-η) obtained from the normalized polarization curves[39,40]. As shown in Fig. 4b, d, the Tafel slope of the Co_3O_4/Fe_3O_4 (4:1) composite is 78 mV dec^{-1}, which is smaller than that of pure mesoporous Co_3O_4 (84 mV dec^{-1}), indicating that the mesoporous Co_3O_4/Fe_3O_4 (4:1) composite is a more efficient catalyst and has favorable kinetics during the OER in alkaline medium.

Chronoamperometric measurements were performed to investigate the long-term durability in the OER. The durability of the electrocatalysts was tested at 10 mA cm^{-2} in 1 M KOH solution at room temperature. As observed in Fig. 5d, both the pure Co_3O_4 and Co_3O_4/Fe_3O_4 (4:1)

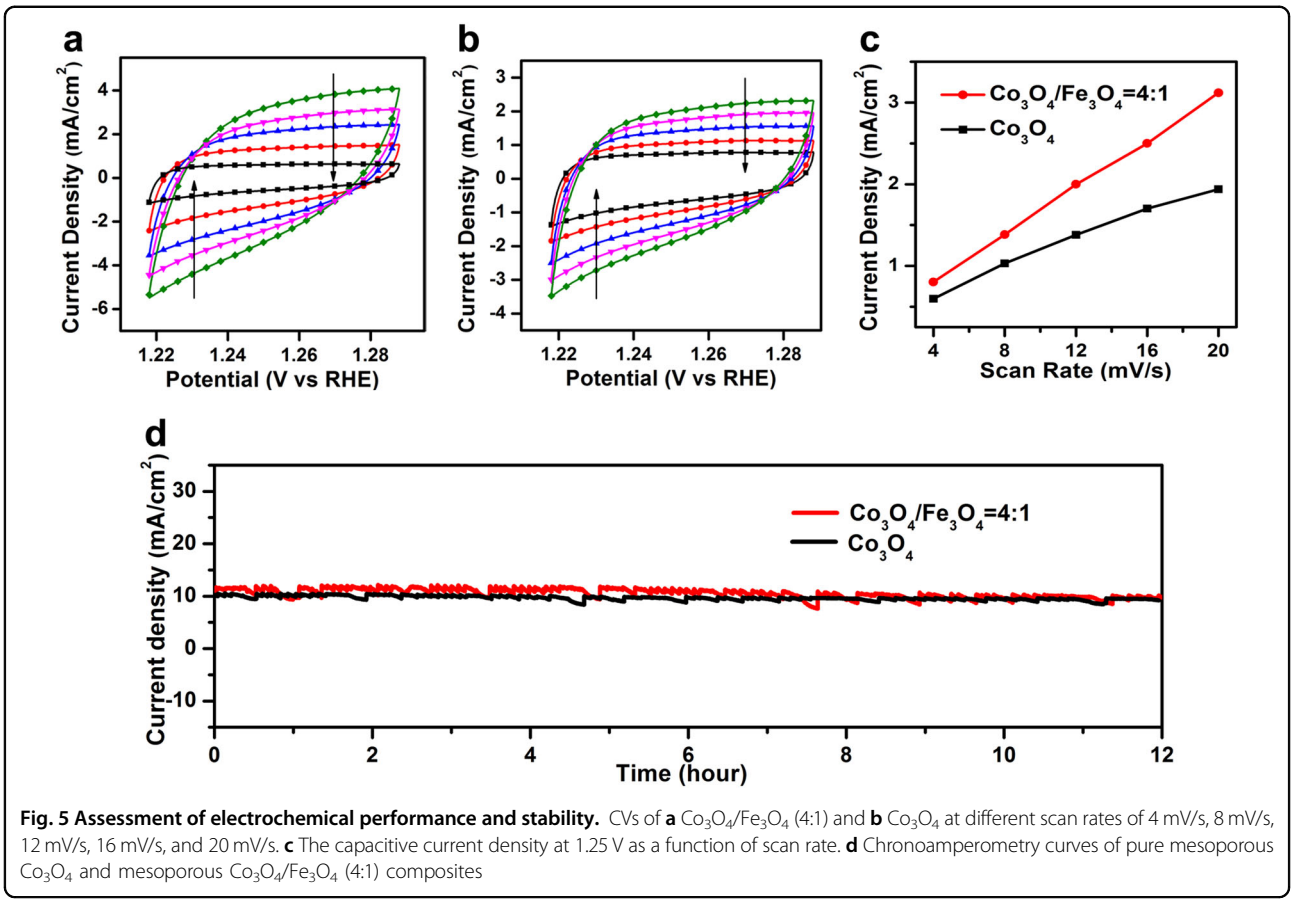

Fig. 5 Assessment of electrochemical performance and stability. CVs of **a** Co_3O_4/Fe_3O_4 (4:1) and **b** Co_3O_4 at different scan rates of 4 mV/s, 8 mV/s, 12 mV/s, 16 mV/s, and 20 mV/s. **c** The capacitive current density at 1.25 V as a function of scan rate. **d** Chronoamperometry curves of pure mesoporous Co_3O_4 and mesoporous Co_3O_4/Fe_3O_4 (4:1) composites

nanocomposite electrodes show excellent electrochemical durability over a 12-h continuous experiment. Their excellent long-term durability can be attributed to the formation of an interconnected metal oxide network after calcination, which is robust enough for the OER. No obvious changes were observed in the TEM image compared with the untested samples (Figure S17), further confirming the robustness of the as-prepared mesoporous Co_3O_4. The slight current density decrease is due to catalysts falling off the glassy carbon electrode during the oxygen evolution process. The excellent electrochemical performance convinces us that a ligand-assisted evaporation-induced self-assembly strategy opens a new way to synthesizing more efficient catalysts for the OER.

Conclusion

In conclusion, a general ligand-assisted self-assembly approach has been demonstrated to synthesize mesoporous transition metal oxides with a high degree of crystallinity. Citric acid or ascorbic acid is employed as a coordination agent, and chelation between the metal and ligand can effectively slow the hydrolysis and condensation rates of the metal precursors. This approach is high yielding (measured in grams) and insensitive to synthesis conditions. Almost all transition metal oxides in the periodic table can be synthesized by this widely applicable method. These obtained mesoporous materials possess high specific surface areas and large pore volumes, which provide abundant reaction sites for the electrolyte, making them possible for use as remarkable electrochemical materials. As a demonstration, the mesoporous Co_3O_4/Fe_3O_4 (4:1) nanocomposite exhibits an exceptional catalytic ability in water splitting with low overpotential (322 mV at 10 mA cm^{-2}), large anodic current, and long-term durability. The present method offers a new way to prepare mesoporous transition metal oxides and multimetal oxide composites for a wide range of applications.

Acknowledgements

This work was supported by the Young Thousand Talented Program and the National Natural Science Foundation of China (21671073, 21621001, and 21671074), the "111" Project of the Ministry of Education of China (B17020), and Program for JLU Science and Technology Innovative Research Team.

Author contributions

Z.A.Q. designed the experiments. D.Y.F. performed the experiments and analyzed the data. T.N.G. and T.W. performed the N_2 adsorption experiments. A.L. and K.Q.L. carried out the TEM imaging. M.H.F. and Q.S.H. discussed the results and commented on the manuscript.

Competing interests
The authors declare no competing interests.

Publisher's note
Springer Nature remains neutral with regard to jurisdictional claims in published maps and institutional affiliations.

Supplementary Information is available for this paper at https://doi.org/10.1038/s41427-018-0072-z.

Received: 8 April 2018 Revised: 21 June 2018 Accepted: 26 June 2018.
Published online: 21 August 2018

References

1. Sarkar, D. et al. A subthermionic tunnel field-effect transistor with an atomically thin channel. *Nature* **526**, 91–95 (2015).
2. Yu, J. et al. Nature-inspired 2D-mosaic 3D-gradient mesoporous framework: bimetal oxide dual-composite strategy toward ultrastable and high-capacity lithium storage. *ACS Nano* **12**, 2035–2047 (2018).
3. Ba, N., Zhu, L., Zhang, G., Li, J. & Li, H. Facile synthesis of 3D CuO nanowire bundle and its excellent gas sensing and electrochemical sensing properties. *Sens. Actuators, B* **227**, 142–148 (2016).
4. Zhu, S. et al. Ultrathin-nanosheet-induced synthesis of 3D transition metal oxides networks for lithium ion battery anodes. *Adv. Funct. Mater.* **27**, 1605017 (2017).
5. Li, G. et al. Pomegranate-inspired design of highly active and durable bifunctional electrocatalysts for rechargeable metal-air batteries. *Angew. Chem. Int. Ed.* **55**, 4977–4982 (2016).
6. Hua, B. et al. A coupling for success: controlled growth of Co/CoO_x nanoshoots on perovskite mesoporous nanofibres as high-performance trifunctional electrocatalysts in alkaline condition. *Nano Energy* **32**, 247–254 (2017).
7. Nasi, L. et al. Mesoporous single-crystal ZnO nanobelts: supported preparation and patterning. *Nanoscale* **5**, 1060–1066 (2013).
8. Ma, Y. et al. A chelation-induced cooperative self-assembly methodology for the synthesis of mesoporous metal hydroxide and oxide nanospheres. *Nanoscale* **10**, 5731–5737 (2018).
9. Namai, A. et al. Hard magnetic ferrite with a gigantic coercivity and high frequency millimetre wave rotation. *Nat. Commun.* **3**, 1035 (2012).
10. Deng, X., Chen, K. & Tüysüz, H. Protocol for the nanocasting method: preparation of ordered mesoporous metal oxides. *Chem. Mater.* **29**, 40–52 (2016).
11. Fu, S. et al. Highly ordered mesoporous bimetallic phosphides as efficient oxygen evolution electrocatalysts. *ACS Energy Lett.* **1**, 792–796 (2016).
12. Lee, J. et al. Direct access to thermally stable and highly crystalline mesoporous transition-metal oxides with uniform pores. *Nat. Mater.* **7**, 222–228 (2008).
13. Fan, J., Boettcher, S. W. & Stucky, G. D. Nanoparticle assembly of ordered multicomponent mesostructured metal oxides via a versatile sol-gel process. *Chem. Mater.* **18**, 6391–6396 (2006).
14. Poyraz, A. S., Kuo, C.-H., Biswas, S., King'ondu, C. K. & Suib, S. L. A general approach to crystalline and monomodal pore size mesoporous materials. *Nat. Commun.* **4**, 2952 (2013).
15. Huang, L. et al. Controlled synthesis and flexible self-assembly of monodisperse Au@Semiconductor core/shell hetero-nanocrystals into diverse superstructures. *Chem. Mater.* **29**, 2355–2363 (2017).
16. Huang, J. et al. Bottom-up assembly of hydrophobic nanocrystals and graphene nanosheets into mesoporous nanocomposites. *Langmuir* **30**, 4434–4440 (2014).
17. Patra, A. K., Das, S. K. & Bhaumik, A. Self-assembled mesoporous TiO2 spherical nanoparticles by a new templating pathway and its enhanced photoconductivity in the presence of an organic dye. *J. Mater. Chem.* **21**, 3925–3930 (2011).
18. Paul, M., Pal, N., Mondal, J., Sasidharan, M. & Bhaumik, A. New mesoporous magnesium–alminum mixed oxide and its catalytic activity in liquid phase Baeyer–Villiger oxidation reaction. *Chem. Eng. Sci.* **71**, 564–572 (2012).
19. Zhang, J. et al. Ligand-assisted assembly approach to synthesize large-pore ordered mesoporous titania with thermally stable and crystalline framework. *Adv. Energy Mater.* **1**, 241–248 (2011).
20. Wang, Z. et al. Controlled synthesis of ordered mesoporous carbon-cobalt oxide nanocomposites with large mesopores and graphitic walls. *Chem. Mater.* **28**, 7773–7780 (2016).
21. Das, S. K., Bhunia, M. K., Sinha, A. K. & Bhaumij, A. Self-assembled mesoporous zirconia and sulfated zirconia nanoparticles synthesized by triblock copolymer as template. *J. Phys. Chem. C.* **113**, 8918–8923 (2009).
22. Zhou, X. et al. Chelation-assisted soft-template synthesis of ordered mesoporous zinc oxides for low concentration gas sensing. *J. Mater. Chem. A* **4**, 15064–15071 (2016).
23. Cai, Z. et al. Single-crystalline ultrathin Co_3O_4 nanosheets with massive vacancy defects for enhanced electrocatalysis. *Adv. Energy Mater.* **8**, 1701694 (2018).
24. Liang, Y. et al. Co_3O_4 nanocrystals on graphene as a synergistic catalyst for oxygen reduction reaction. *Nat. Mater.* **10**, 780–786 (2011).
25. Khalid, M., Honorato, A. M. B., Varela, H. & Dai, L. Multifunctional electrocatalysts derived from conducting polymer and metal organic framework complexes. *Nano Energy* **45**, 127–135 (2018).
26. Subbaraman, R. et al. Trends in activity for the water electrolyser reactions on 3d M (Ni,Co,Fe,Mn) hydr(oxy)oxide catalysts. *Nat. Mater.* **11**, 550–557 (2012).
27. Wang, Y. et al. Bio-inspired leaf-mimicking nanosheet/nanotube heterostructure as a highly efficient oxygen evolution catalyst. *Adv. Sci.* **2**, 1500003 (2015).
28. Wang, H., Zhuo, S., Liang, Y., Han, X. & Zhang, B. General self-template synthesis of transition-metal oxide and chalcogenide mesoporous nanotubes with enhanced electrochemical performances. *Angew. Chem. Int. Ed.* **55**, 9055–9059 (2016).
29. Tung, C.-W. et al. Reversible adapting layer produces robust single-crystal electrocatalyst for oxygen evolution. *Nat. Commun.* **6**, 8106 (2015).
30. Zhang, X. et al. Effective construction of high-quality iron oxy-hydroxides and Co-doped iron oxy-hydroxides nanostructures: towards the promising oxygen evolution reaction application. *Sci. Rep.* **7**, 43590 (2017).
31. Xu, W. et al. Porous cobalt oxide nanoplates enriched with oxygen vacancies for oxygen evolution reaction. *Nano Energy* **43**, 110–116 (2018).
32. Zhuang, L. et al. Ultrathin iron-cobalt oxide nanosheets with abundant oxygen vacancies for the oxygen evolution reaction. *Adv. Mater.* **29**, 1606793 (2017).
33. Pan, Y. et al. Core-shell ZIF-8@ZIF-67-derived CoP nanoparticle-embedded N-doped carbon nanotube hollow polyhedron for efficient overall water splitting. *J. Am. Chem. Soc.* **140**, 2610–2618 (2018).
34. Wang, J. et al. Synergistic effect between metal-nitrogen-carbon sheets and NiO nanoparticles for enhanced electrochemical water-oxidation performance. *Angew. Chem. Int. Ed.* **54**, 10530–10534 (2015).
35. Wu, A. et al. Integrating the active OER and HER components as the heterostructures for the efficient overall water splitting. *Nano Energy* **44**, 353–363 (2018).
36. Deng, S. et al. Hollow $TiO_2@Co_9S_8$ core-branch arrays as bifunctional electrocatalysts for efficient oxygen/hydrogen production. *Adv. Sci.* **5**, 1700772 (2018).
37. Deng, S. et al. Directional construction of vertical nitrogen-doped 1T-2H $MoSe_2$ /graphene shell/core nanoflake arrays for efficient hydrogen evolution reaction. *Adv. Mater.* **29**, 1700748 (2017).
38. Yu, M. et al. Dual-doped molybdenum trioxide nanowires: a bifunctional anode for fiber-shaped asymmetric supercapacitors and microbial fuel cells. *Angew. Chem. Int. Ed.* **55**, 6762–6766 (2016).
39. Zhang, Y. et al. 3D porous hierarchical nickel-molybdenum nitrides synthesized by RF plasma as highly active and stable hydrogen-evolution-reaction electrocatalysts. *Adv. Energy Mater.* **6**, 1600221 (2016).
40. Cao, L.-M., Wang, J.-W., Zhong, D.-C. & Lu, T. –B. Template-directed synthesis of sulphur doped NiCoFe layered double hydroxide porous nanosheets with enhanced electrocatalytic activity for the oxygen evolution reaction. *J. Mater. Chem. A* **6**, 3224–3230 (2018).